Journal of Power Sources 196 (2011) 1541–1554

Contents lists available at ScienceDirect

Journal of Power Sources

journal homepage: www.elsevier.com/locate/jpowsour

Lead-acid batteries in micro-hybrid applications. Part I. Selected key parameters

S. Schaeck[a,*], A.O. Stoermer[a], F. Kaiser[a], L. Koehler[b], J. Albers[c], H. Kabza[d]

[a] BMW Group, 80788 München, Germany
[b] Hochschule München, 80335 München, Germany
[c] Johnson Controls Power Solutions EMEA, 30419 Hannover, Germany
[d] Universität Ulm, Institut für Energiewandlung und -speicherung, 89081 Ulm, Germany

ARTICLE INFO

Article history:
Received 5 July 2010
Received in revised form 24 August 2010
Accepted 25 August 2010
Available online 29 September 2010

Keywords:
Valve-regulated lead-acid battery (VRLA)
Micro-hybrid electric vehicle
Dynamic charge acceptance
Overcharge
Overdischarge

ABSTRACT

Micro-hybrid electric vehicles were launched by BMW in March 2007. These are equipped with brake energy regeneration (BER) and the automatic start and stop function (ASSF) of the internal combustion engine. These functions are based on common 14 V series components and lead-acid (LA) batteries. The novelty is given by the intelligent onboard energy management, which upgrades the conventional electric system to the micro-hybrid power system (MHPS). In part I of this publication the key factors for the operation of LA batteries in the MHPS are discussed. Especially for BER one is high dynamic charge acceptance (DCA) for effective boost charging. Vehicle rest time is identified as a particular negative parameter for DCA. It can be refreshed by regular fully charging at elevated charge voltage. Thus, the batteries have to be outstandingly robust against overcharge and water loss. This can be accomplished for valve-regulated lead-acid (VRLA) batteries at least if they are mounted in the trunk. ASSF goes along with frequent high-rate loads for warm cranking. The internal resistance determines the drop of the power net voltage during cranking and is preferably low for reasons of power net stability even after years of operation. Investigations have to be done with aged 90 Ah VRLA–absorbent glass mat (AGM) batteries. Battery operation at partial state-of-charge gives a higher risk of deep discharging (overdischarging). Subsequent re-charging then is likely to lead to the formation of micro-short circuits in the absorbent glass mat separator.

© 2010 Elsevier B.V. All rights reserved.

1. Introduction

In March 2007 the BMW Group has launched the micro-hybrid functions brake energy regeneration (BER) and automatic start and stop function (ASSF), which are stepwise rolled out to the entire fleet of vehicles with 14 V power system. Valve-regulated lead-acid (VRLA) batteries with absorbent glass mat (AGM) technology are applied. Thus, the lead-acid (LA) battery acts as key component for reduction of fuel consumption and CO_2 emissions in micro-hybrid electric vehicles (HEVs), which represent the lowest level of vehicle powertrain electrification.

The micro-hybrid power system (MHPS) is extensively discussed e.g. in [1–4]. The main aspects are shortly summarized here to enhance the understanding of the argumentation in this publication: ASSF and BER are part of an intelligent energy management which controls energy and communication flow in the vehicle power net. The battery is equipped with an intelligent battery sensor (IBS) for logging critical battery parameters. ASSF switches off the engine at idle and the internal combustion engine (ICE) is automatically restarted by the driver's or the power management's request. Thus, the number of high-rate discharges is significantly higher compared to the conventional power system (CPS). In the BER function the battery is operated in partial state-of-charge (pSoC). In coasting and braking phases the output voltage of the alternator is elevated in order to 'boost'-charge the battery without fuel consumption. The necessary dynamic charge acceptance (DCA) represents a paradigm shift of operating LA batteries. The former operation strategy aiming at a fully charged SLI (starting, lighting, ignition) battery has changed to a more sophisticated strategy, which is directly linked to the operational mode of the vehicle.

This makes the LA battery a key component of the micro-hybrid architecture. As the SLI functions remain unchanged, the MHPS means additional requirements for the VRLA–AGM battery [5]. Because of the fact that the LA battery is a very prominent spare part in the automotive industry and the main root cause for vehicle breakdowns [6,7], some of these aspects like sulphation at pSoC (e.g. [5,8]), charge acceptance (e.g. [9,10]) or heat tolerance [11] were already in the focus of previous experimental investigations. The spectrum of experiments reaches from research contributions on battery components, especially electrode materials (e.g. [12]), to bench tests [5] and statistical field tests [13,14]. Based on these contributions several key parameters for the application

* Corresponding author. Tel.: +49 89 382 78653; fax: +49 89 382 42827.
E-mail addresses: stefan.schaeck@bmw.de, stefan.schaeck@gmx.de (S. Schaeck).

0378-7753/$ – see front matter © 2010 Elsevier B.V. All rights reserved.
doi:10.1016/j.jpowsour.2010.08.077

of VRLA–AGM batteries in micro-HEVs have emerged. In the following these items are discussed by means of investigations performed in the BMW laboratories.

2. Dynamic charge acceptance

The efficiency of BER depends very strongly on battery DCA as it limits the regenerated amount of charge during boost charging. Due to the permanently 'full charge' operational strategy in the CPS even the stationary charge acceptance was regarded as a less important battery feature. Recently, DCA has turned from an underestimated to a highly important parameter in the automotive and battery industry [10]. So far, various publications aimed at a generally increased level of charge acceptance of LA batteries by the admixture of carbon in the negative active mass (NAM) [15]. Hereby, different forms of carbon are in the focus of current research with different modes of effects like enhancement of the overall conductivity for higher charge currents, reduction of the reaction rate of hydrogen evolution or acceleration of acid diffusion in the NAM pores [16,17]. In the application of LA batteries in a micro-HEV one of the key effects is related to the use of conductive carbon black, which was demonstrated by Shiomi et al. [18]. It was shown that carbon slows down the formation of large $PbSO_4$ crystals.

2.1. Influence of rest time

The investigation described in this section demonstrates that preservation of a certain level of charge acceptance has to be the main focus in automotive application. A 90 Ah VRLA–AGM battery (released state-of-the-art design from an OEM supplier) is conditioned to a certain SoC level by discharging with I_5. Then, after a certain rest time t_{rest}, DCA is measured by applying the charge voltage $U = 14.8$ V for the duration of $t_{charge} = 60$ s. In order to reflect the customer use case the rest time was varied in a series of measurements from seconds to one week. The series was done at 90%, 80%, 70% and 60% SoC with a fixed rest period t_{rest}. The batteries were *IU*-charged ($U = 14.8$ V, $I = I_5$, $t = 24$ h) before the next SoC series was performed with another fixed rest time. In Fig. 1 the dependency of DCA versus rest time t_{rest} is depicted for SoC = 90%.

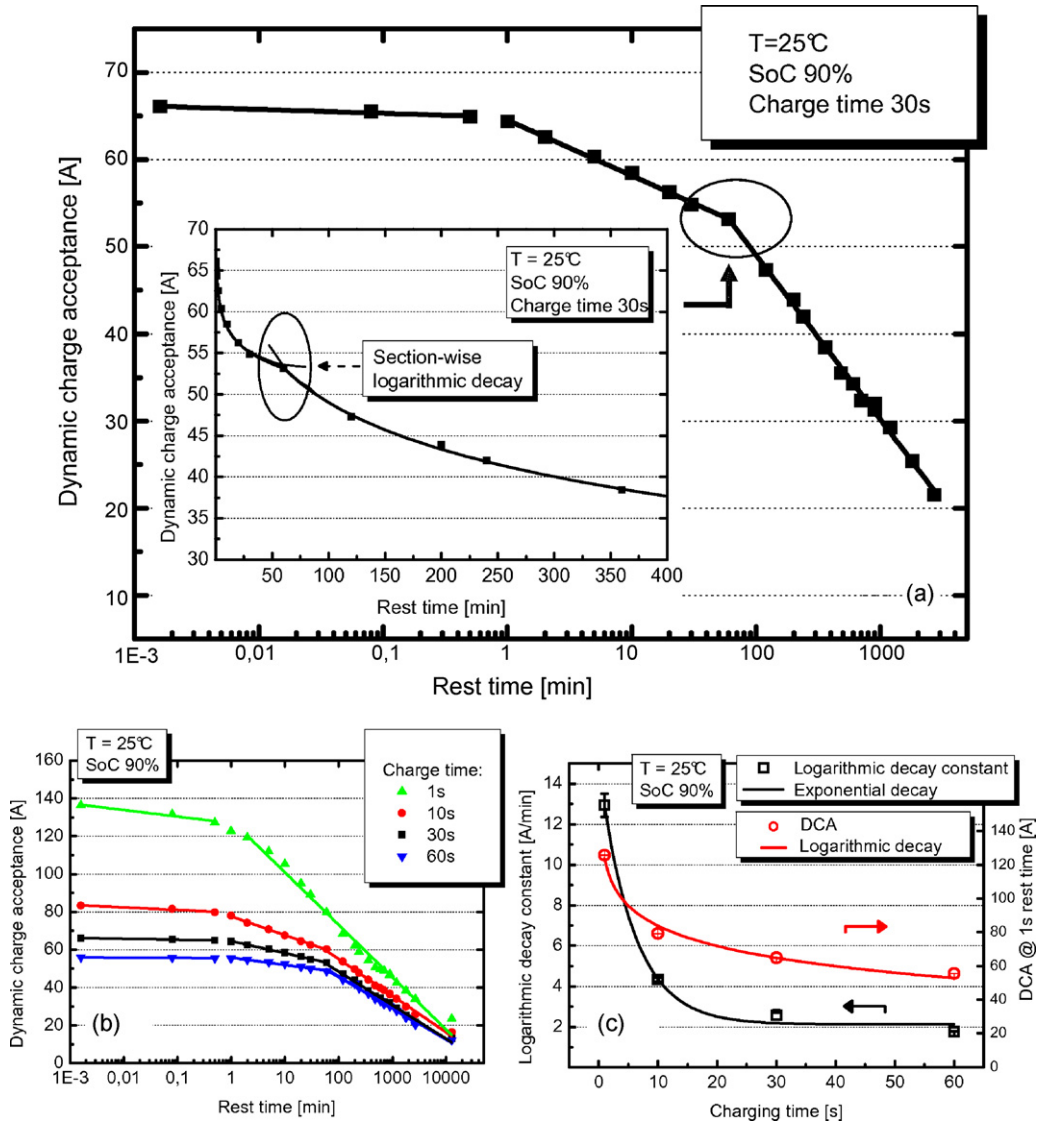

Fig. 1. (a) Dynamic charge acceptance at $U = 14.8$ V versus rest time. For a SoC adjusted to 90% the charge current at $t_{charge} = 30$ s is illustrated. According to the inset, which shows a section-wise logarithmic decay as a function of rest time, two linear gradients appear in a *x*-logarithmic plot. (b) The transition at $t_{rest} \approx 60$ min is more significant with increasing charging time. A further transition was found at $t_{rest} \approx 1$ min. (c) The logarithmic DCA decay constants b_{DCA} (fitted for 1 min $\leq t_{rest} \leq$ 60 min) behave exponentially versus charging time (squares), which negatively affects the BER efficiency in the MHPS.

The charge current was measured after t_{charge} = 30 s with reference to the charge trigger. The amount of accepted current decreases with increasing rest time (see inset). Data fitting suggests a logarithmic decay, i.e. DCA $\propto -b_{DCA}$[A min^{-1}]ln(t_{rest}). As indicated by the circle in the inset, the data were fitted section-wise since two different DCA decay regimes, b_{DCA} [A min^{-1}], were found. By plotting the curves on a logarithmic x-scale, straight lines with different slopes b_{DCA} are obtained (main figure). It has to be noted that for long rest times the curve is expected to converge to the x-axis in a left bend also in the log-plot. However, the corresponding s-shaped curves were not found in the chosen observation period. The transitions between the different slopes in Fig. 1(a) occur in a narrow time window, which is comparable to the data sampling rate. Consequently, the (continuous) transition appears like an unsteadiness in the chosen plot style. In further discussion the term 'kink' addresses the transition between two decay regimes with different slopes. The correlation coefficients R^2 of the section-wise fits are greater than 0.98. In addition to the unsteadiness at about t_{rest} = 60 min (as highlighted), a second one was found after about 1 min of rest time. However, as only three data points contribute to DCA on the short time scale, the corresponding fit is doubtful. Fig. 1(a) indicates that three sequential mechanisms determine battery charge acceptance in this experiment. Also for varying charge time three sections with comparable R^2 are observed in Fig. 1(b). There is no temporal shift of the sections in dependence of $t_{charge.}$ Only for t_{charge} = 1 s the second 'kink' does not appear.

Qualitatively, the observed behaviour is linked to the dissolution of lead sulphate at the negative electrode (NE) as limiting step. DCA is strongly dependent on the lead sulphate surface which is considerably affected by the previous discharge step and the rest time [19–22]. The behaviour of lead sulphate at the NE is described by Yamaguchi et al. [21,22] (see Fig. 2). A large number of small lead sulphate crystals (a) form a few large crystals (c) during rest time (b) due to lower surface energy and lower crystal binding energy. This recrystallisation process results in lead sulphate with lower chemical reactivity due to worse surface/volume ratio. During charging, the solubility of lead sulphate in sulphuric acid determines the saturation concentration of Pb^{2+} ions. This saturation concentration depends on temperature and acid specific gravity. Furthermore, size and total volume of $PbSO_4$ are critical for the solubility. If the concentration of Pb^{2+} ions drops below the saturation concentration due to battery charging, lead sulphate is dissolved. The resulting concentration (diffusion) overpotential ΔU_{conc} is given as

$$\Delta U_{conc} \propto \frac{RT}{nF} \ln\left(\frac{c_{Pb^{2+}}}{c^0_{Pb^{2+}}}\right) \quad (1)$$

with the equilibrium concentration $c^0_{Pb^{2+}}$ and the actual concentration of Pb^{2+} ions $c^{Pb^{2+}}$ [23]. As U-charging is applied in the presented experiment, increasing ΔU_{conc} results in decrease of effective charge potential and a logarithmic DCA loss in first approximation. This behaviour is fitted versus t_{charge} in Fig. 1(c) on the right y-axis. A logarithmic current decay of first order was fitted according to DCA$_{t_{rest}=1\,s} \propto -$const. ln($t_{charge}$) with R^2 = 0.96.

The described behaviour of DCA versus t_{rest} is not yet fully understood. Hereby, the influence of t_{rest} on the term $c_{Pb^{2+}}/c^0_{Pb^{2+}}$ in Eq. (1) for subsequent charging has to be discussed. A promising approach is given by the 'hardening crystals' model by Thele et al. [19] and Sauer [24]. The approach links the concentration of Pb^{2+} ions in the charging step in Eq. (1) after recrystallisation (during t_{rest}) with their solubility [19], which is determined by the radii distribution of the recrystallised lead sulphate [25]. Up to t_{rest} = 3 h Thele et al. could demonstrate quite good agreement of simulated and measured DCA. However, both the influence of short term history (twice as high DCA following discharging instead of charging [10]) and the effects of prolonged rest times are not satisfactorily described by Thele's model [26]. Especially, the 'kink'-like transitions in Fig. 1, which allow the section-wise fitting, are not fully understood.

A phenomenological approach for explanation is given as follows: The transition of the gradients in Fig. 1(a) at about t_{rest} = 60 min suggests a particular crystal radius during the recrystallisation process as was illustrated in Fig. 2. If the volume/surface ratio exceeds a particular value, the release of Pb^{2+} ions to the electrolyte is extremely impeded [27]. Then, the charge potential

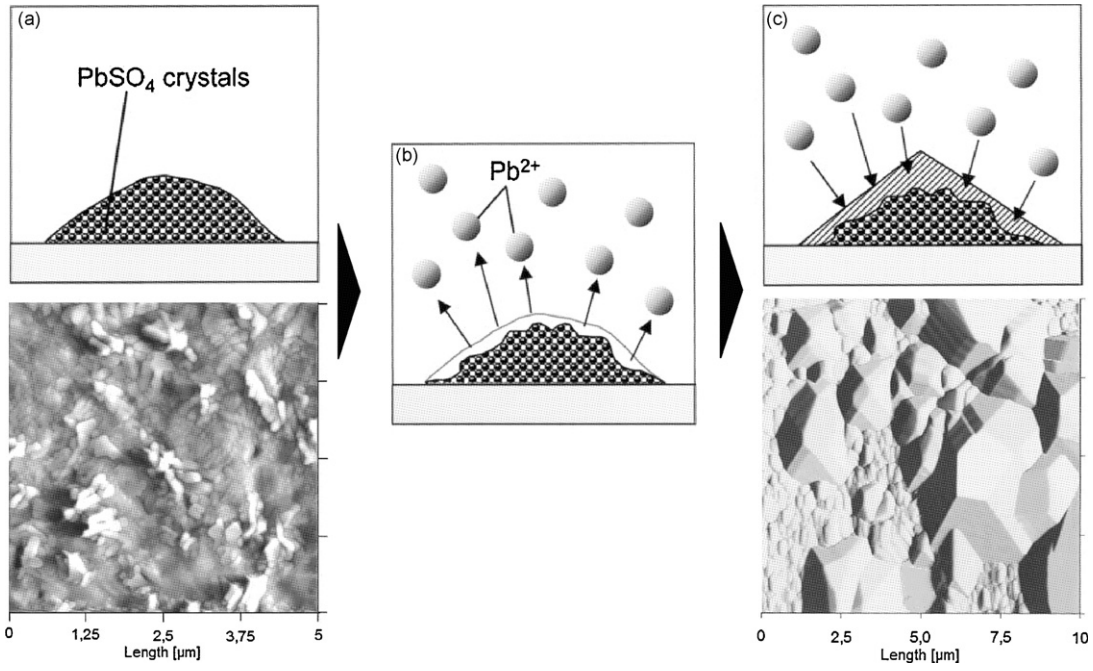

Fig. 2. (a) Lead sulphate precipitates at the NE during battery discharge. According to the mechanism of Ostwald ripening (dissolution and re-precipitation), new crystals form on the old ones under conservation of volume and reduction of surface (b and c) [21]. In the experiment by Yamaguchi et al., sulphuric acid with rather low concentration (0.05 mol l^{-1}) was used in order to accelerate the process for in situ AFM observation ([22] and [21], modified).

is dominated by the diffusion and charge transfer overpotentials. Two fundamental prerequisites are accompanied with this train of thoughts: Firstly, the recrystallisation rate has to be homogenous across the plates. Secondly, the origin for recrystallisation processes has to be characterised by homogeneously distributed 'seed crystals' concerning both local and size distribution. Otherwise, even if such a critical volume/surface ratio exists, a broad transition area would be observed instead of a 'kink'-like transition in a shorter time window. Fig. 1(b) may be consistent with this explanation: The DCA transition at about t_{rest} = 60 min is not observed for charging time t_{charge} = 1 s. Independent of rest time, the number of smaller crystals is sufficient to ensure DCA within the first second of charge. Due to recrystallisation also these crystals grow larger, their density decreases and, therefore, DCA at t_{charge} = 1 s. After more than 60–100 min of t_{rest} the number of smaller crystals falls below a particular level so that after $t_{charge} \geq 10$ s only larger crystals dominate charge acceptance. With increasing rest time these unreactive crystals grow larger as well and the already low DCA is further reduced.

It is also observed in Fig. 1(b) that DCA decreases noticeably for t_{charge} = 1 s within the first minute of rest time. This is related to the diffusion overpotential at turn-off of discharge current (low SO_4^{2-} concentration in the pores). On the time scale of seconds to minutes the (asymptotic) diffusion overpotential decrease is most significant and the initial effective charging potential at charging is reduced by rest time [28]. After about t_{rest} = 1 min and t_{charge} = 1 s the regime of reversed diffusion effects is reached (high SO_4^{2-} concentration in the pores) and DCA turns into the second section. In this second section (1 min $\leq t_{rest} \leq$ 60 min) the logarithmic DCA decays are fitted in Fig. 1(b) ($R^2 \geq 0.97$) and the decay constant b_{DCA} according to $DCA \propto -b_{DCA}[A\,min^{-1}]\ln(t_{rest})$ is given in Fig. 1(c) on the left y-axis versus t_{charge}. It is observed that b_{DCA} decays exponentially with charge time according to $b_{DCA}[A\,min^{-1}] \propto \exp(-t_{charge}/const.)$. Consequently, an increase of t_{rest} has the greatest impact on DCA decrease especially at short charging time. For example, after $t_{rest} \approx$ 10,000 min it is observed that $DCA(t_{charge} = 1\,s) \approx DCA(t_{charge} = 60\,s)$. For the application of VRLA–AGM batteries in a passenger vehicle this means that after a vehicle rest time of about one week the initial DCA on the time scale of a few seconds reaches the level of stationary charge acceptance. This is of major importance for BER since the amount of regenerated energy results from DCA within a few seconds of throttle cut-off. Following a vehicle rest time of about one week, the initially accepted current during regenerative charging is at a low level

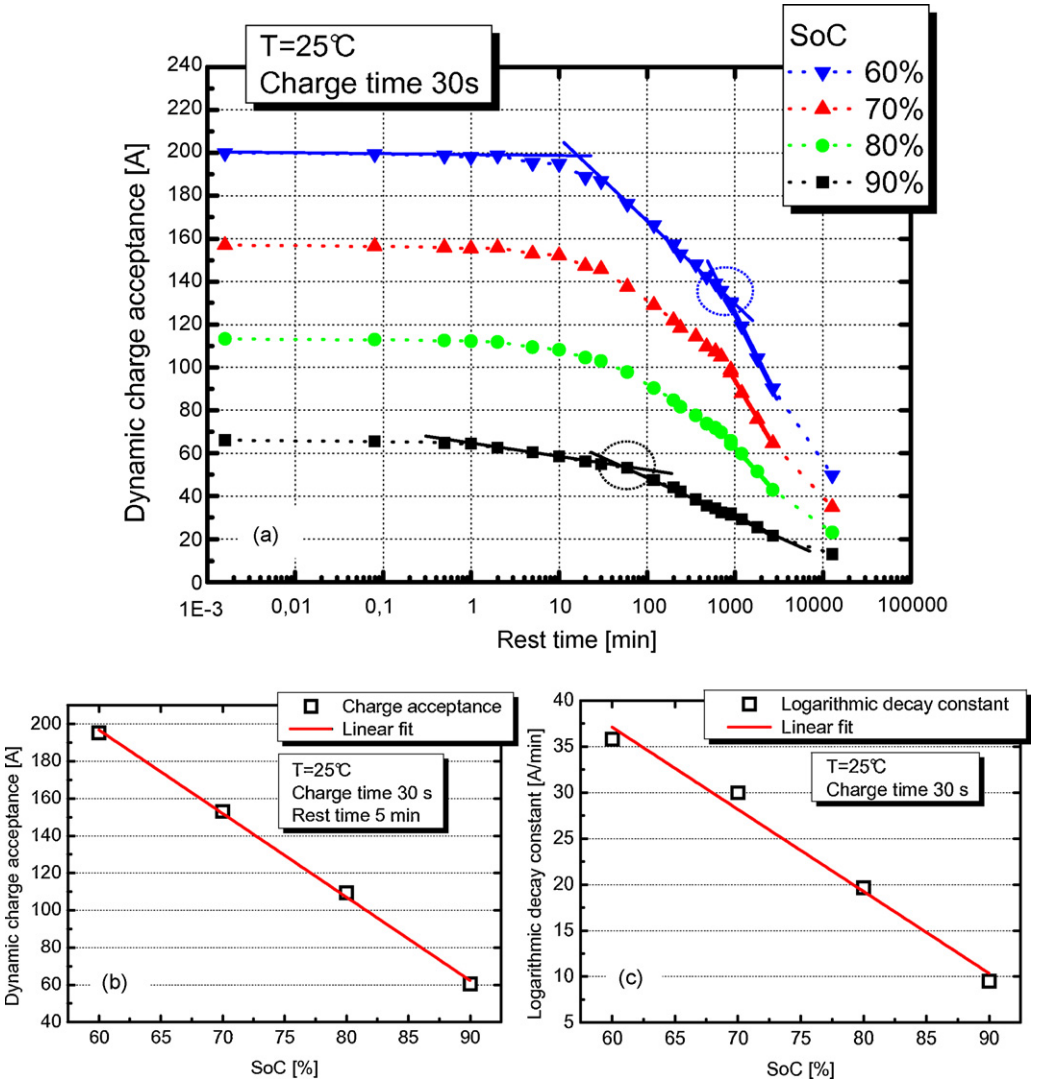

Fig. 3. (a) Dynamic charge acceptance as a function of rest time and varying SoC. It has to be noticed that the charge current limit of 200 A is reached at SoC = 60%. The multiple regime behaviour is also found at different SoCs. As highlighted by the circles, the second transition shifts to higher rest time with increasing SoC. (b) The charge acceptance decreases linearly with SoC at a fixed rest time due to decreased effective charge potential. (c) The logarithmic DCA decay rate was fitted for t_{rest} > 1000 min and shows linear behaviour with SoC.

of DCA < 20 A. As described in [5], a refresh function is applied in conjunction with BER. This function fully charges the battery with elevated charge voltage in order to re-activate the lead sulphate. The refresh function is triggered by a combined counter, which includes also the vehicle rest time as input variable. The aspect of refreshing will be picked up later again.

In Fig. 3 the effect of SoC on rest time dependent DCA is depicted. The data for SoC = 90% correspond to Fig. 1. Due to scaling of the ordinate, the different linear sections of the SoC = 90%-curve are not clearly visible. However, the multi-regime behaviour is also found at lower SoC as indicated for SoC = 60%. It has to be noticed that the second transition shifts to higher rest time with decreasing SoC. As highlighted by the circles in Fig. 3(a), the 'kink' occurs by one order of magnitude later in the case of SoC = 60% compared to SoC = 90%. Within the presented phenomenological explanation model, the solubility of lead sulphate in dependence of the acid density has to be taken into consideration. At room temperature the solubility of $PbSO_4$ at SoC = 60% is roughly twice as high as for SoC = 90% [29]. This results in two opposing modes of action. On the one hand, the recrystallisation rate is increased with lower SoC. On the other hand, the size of deposited lead sulphate crystals is expected to be larger as well. Furthermore, the charge potential at $U = 14.8$ V is effectively higher. In total, these phenomena obviously result in a shift of the transition of the DCA decay constants to higher t_{rest} with decreasing SoC. In Fig. 3(b) the absolute DCA values are given versus SoC at $t_{charge} = 30$ s and $t_{rest} = 5$ min. The linear decrease is about −45 A per +10% SoC, which is linked to the loss of effective charge potential with increasing SoC. The logarithmic DCA decay is fitted in Fig. 3(a) in the last section, i.e. for $t_{rest} > 1000$ min, and the decay rates b_{DCA} are shown in Fig. 3(c). It is observed that the decay rate decreases linearly with SoC. This means that the benefit of higher DCA at lower SoC rapidly vanishes with vehicle rest time. Nevertheless, DCA is still three times higher at SoC = 60% than at SoC = 90% after about one week rest time. This would suggest to decrease the pSoC operation level of BER in order to gain higher regenerative efficiency. However, it is seen in ongoing, not yet published work based on [5] that such a strategy is detrimental for battery cycle life.

Finally, the influence of temperature on DCA is illustrated by Fig. 4. The graphs are given for SoC = 80% and the curve at $T = 25\,^{\circ}C$ is taken from Fig. 3(a). In the first regime and below room temperature DCA increases with increasing rest time. It is supposed that heat distribution effects, which occur after discharge with I_5, might positively influence DCA in the first seconds of rest time when heat propagates from the top lead to the electrodes. Such an effect was observed by Yamaguchi et al. in a similar experiment [21]. The qualitative explanation by Yamaguchi is also based on a two-step process that divides a single lead sulphate crystal into an unreactive covering part and a more reactive core part. Furthermore, it can be seen by Fig. 4 that higher temperature causes shifting of the transition area to higher t_{rest} (highlighted by circles). Similar to the discussion of Fig. 3, opposing effects have to be regarded. Increased temperature promotes the formation of unreactive lead sulphate crystals as well as the reactivity during charging.

In summary, it was demonstrated so far that absolute DCA covers about one order of magnitude in dependence of the parameters SoC (60–90%), temperature (−18 °C to 25 °C) and rest time (up to one week). DCA drops to about 30–40 A for a brand-new 90 Ah VRLA–AGM battery after only 12 h rest time at 'standard' BER conditions, i.e. $t_{charge} = 10$ s, SoC = 80% and $T = 25\,^{\circ}C$.

2.2. Refresh function

It was demonstrated in [5] by bench test measurements that regular application of a refresh function successfully recovers battery DCA even for cycled batteries and prolonges battery cycle life in pSoC operation. In this section the effects of refreshing and rest time are discussed based on data acquisition in experimental vehicles. Several vehicles equipped with measurement equipment were operated for two years. The collected data comprises around 300 000 km and more than 500 000 boost charge actions. The experimental vehicles were driven regularly with a customer-oriented profile. The target parameter was DCA during regenerative braking. For reason of comparability, the measured DCAs ($t_{charge} = 5$ s) were normalised regarding temperature and SoC. In Fig. 5 an example for such a normalised DCA ($T = 25\,^{\circ}C$ and SoC = 80%) is given for a 90 Ah VRLA–AGM battery with already 80 full cycles in a BMW 6 series car. The DCA average is given on the basis of five days before the refresh (green). The DCA during the refresh is shown in blue. Of course, DCA is worse at the end of the refresh due to the high SoC. After the refresh the SoC is decreased to the pSoC level again and DCA is given during boost charging (red, $t_{charge} = 5$ s). Fitting of an exponential first order decay was performed for the days of operation after the refresh. In a statistical evaluation (70 refresh chargings)

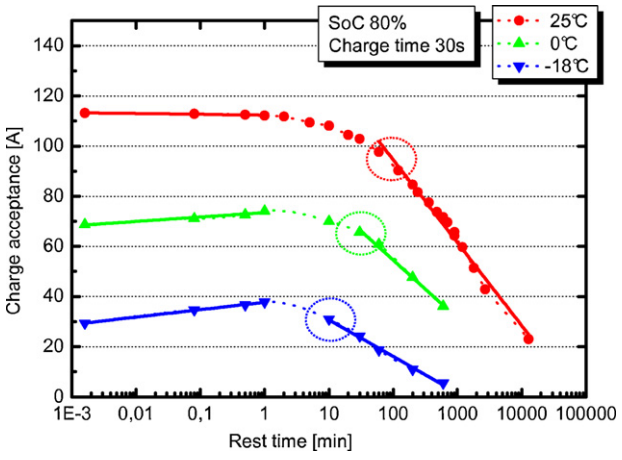

Fig. 4. The influence of temperature on dynamic charge acceptance is depicted versus rest time at SoC = 80% and $t_{charge} = 30$ s. Again, at least a two-stage behaviour is observed. With increasing temperature the transition area shifts to longer rest time t_{rest} because of enhanced reactivity (indicated by the circles).

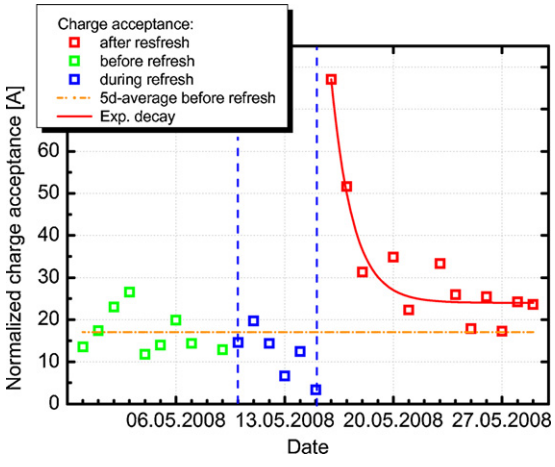

Fig. 5. Example for the short term effect of the battery refresh function derived in a test vehicle. The normalised battery charge acceptance (to SoC = 80% and $T = 25\,^{\circ}C$) before (left, green), during (centre, blue) and after (right, red) the battery refresh charging. According to the intention of the refresh, DCA is maximal after the refresh. The factor of DCA improvement and the duration of the effect were investigated for nearly 70 refresh actions (here one exemplary refresh given). (For interpretation of the references to colour in this figure legend, the reader is referred to the web version of the article.)

both the duration of the refresh (fully charged battery as termination criterion), the factor of DCA improvement (maximum DCA after refresh compared to 5d-average before refresh) and the duration of DCA improvement (intersect of exponential decay after refresh with 5d-average before refresh) were analysed. In less than 5% of all refresh chargings the energy balance was negative, i.e. the gain of DCA (and additionally regenerated energy referred to the DCA level before the refresh) could not compensate the energy consumption during refresh. In the best cases only 5% of the additionally regenerated energy was consumed during the refresh before. As a result, the positive energy balance of a battery refresh and its contribution to the potential for fuel consumption of BER was proven. However, duration and sustainability of the refreshing effect are limited by vehicle rest times. Only one third of refreshes resulted in improvement of DCA that lasted longer than 10 days after termination of the refresh. The vehicles were usually not driven at night and therefore had regularly rest times for more than 12 h.

The presented experiments lead to the conclusion that the optimization of maximum DCA of VRLA–AGM batteries is of secondary importance. Instead, in automotive application the main challenge for improved AGM batteries is to slow down the loss of DCA during rest time at pSoC. According to recent publications on additives in the NAM (e.g. [15,30]), these two goals are not in contradiction, of course. However, the focus widens from electrochemically active and high-surface carbons also to lignosulfonates and $BaSO_4$ [31].

3. Overcharge robustness

For boost charging the battery is subject to an elevated voltage level in BER [5]. By intention, the operational strategy of BER includes deviations from the conventional temperature-dependent charge voltage characteristics. This is also valid for the refresh function. The charge potential $U = 14.8$ V is applied in the entire temperature range and maintained especially at elevated temperature.

The impact of elevated charge voltage at elevated temperature on AGM batteries is investigated in this section. Overcharge phenomena are well known in flooded batteries and take effect by corrosion of the lead alloy of the positive grid [29]. Also decomposition of electrolyte takes place by electrolysis. This affects flooded batteries by far less as these are produced with a reserve of electrolyte. In contrast, the amount of electrolyte in VRLA–AGM batteries, i.e. the saturation of plates and separators with electrolyte, is a parameter, which has to be adjusted exactly in battery

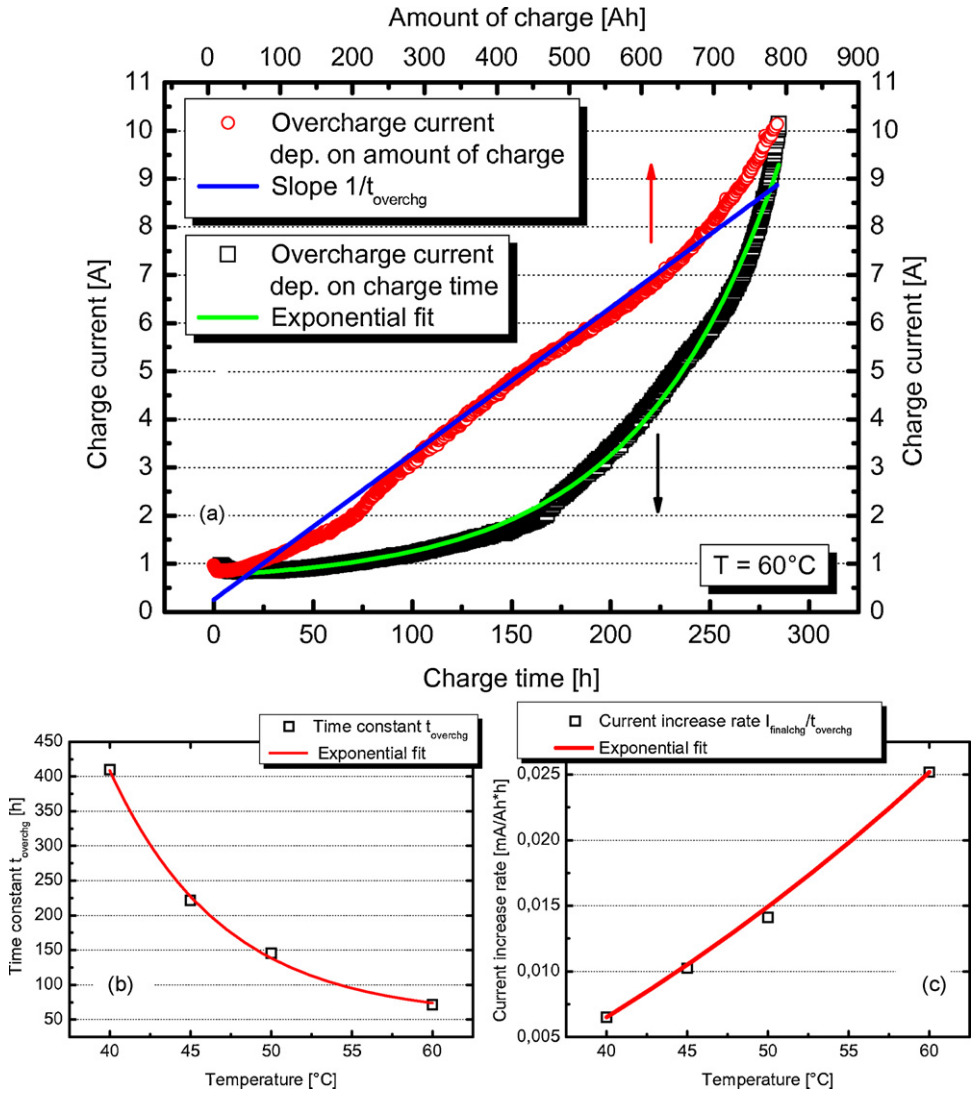

Fig. 6. (a) In an overcharge experiment ($T = 60\,^{\circ}C$) the charge current increases exponentially with overcharge time and linearly with the amount of charge, respectively. (b) The time constants of the exponential current increase are shown for different temperatures in (b) and reveal an exponential decay. (c) In contrast, the current increase rate, normalised to C_{nom}, behaves almost linearly.

production. Thus, VRLA–AGM batteries are much more sensitive to overcharging in terms of water loss than flooded batteries.

The experiments described in this section consist of continually *U*-charging 90 Ah VRLA–AGM batteries with $U = 14.8$ V (like boost charging and refresh function) at different temperatures. In Fig. 6(a) the evolution of overcharge current $I_{overchg}$ at $T = 60\,^{\circ}C$ is depicted versus charge time (bottom *x*-axis) and amount of charge (top *x*-axis). After about 278 h of charging the termination criterion defined in this experiment ($I_{overchg} \geq 8$ A) was reached. The current $I_{overchg}$ increases exponentially ($R^2 = 0.995$) with charge time according to $I_{overchg} \propto I_{finalchg}\exp(t/t_{overchg})$ with the time constant $t_{overchg}$. The overcharge current is based on the final charge current $I_{finalchg}$ of *U*-charging for 24 h. For example, $I_{finalchg}$ was fitted as 240 mA in Fig. 6(a), which matches the final charge current after 24 h-*IU*-charging of a discharged battery. The amount of overcharge $Q_{overchg}(t)$ is proportional to the integral $\int I_{finalchg}\exp(t/t_{overchg})dt \propto I_{overchg}(t)t_{overchg}$. Consequently, the current $I_{overchg}$ is expected to increase linearly with the amount of charge $Q_{overchg}$ and the slope $1/t_{overchg}$. For $T = 60\,^{\circ}C$ this slope is given in Fig. 6(a) and matches the measured curve. In Fig. 6(b) the time constants $t_{finalchg}$ are given for all measured temperatures. It is observed that temperature also exponentially affects $t_{overchg}$. In Fig. 6(c) the associated current increase rate $I_{finalchg}/t_{overchg}$ is depicted, which follows from $dI_{overchg}/dt \propto I_{finalchg}/t_{overchg}\exp(t/t_{overchg})$. Finally, with reference to C_{nom} in Fig. 6(c), the current increase rate shows an almost

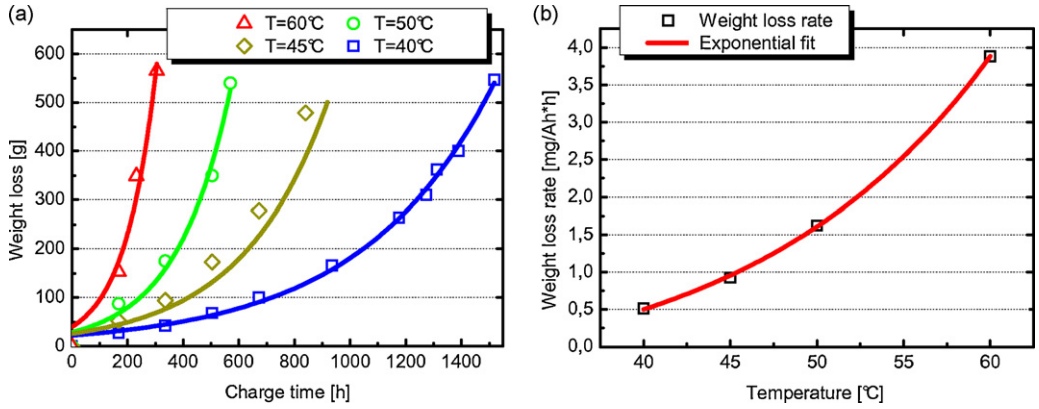

Fig. 7. The overcharged batteries were regularly weighed during the overcharging experiment. Analogous to Fig. 6, m_{Loss} increases exponentially with charge time (a), as does the weight loss rate with temperature (b).

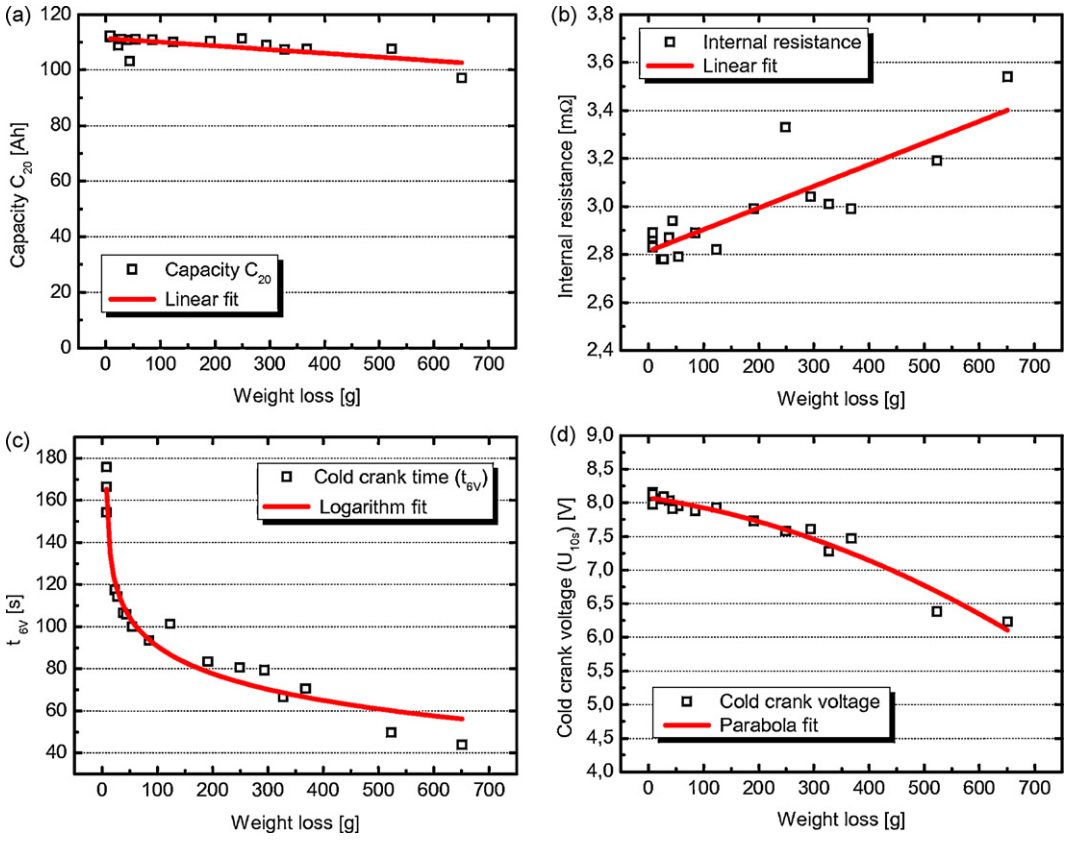

Fig. 8. Important battery parameters were investigated dependent on the weight loss of about 15 batteries. (a) Capacity loss is not predominant, however, internal resistance (b) and the cold crank behaviour (c and d) according to DIN EN 50342-1 show a strong performance loss. It has to be noted that the parameter t_{6V} (c) is not only influenced by water loss, but mainly by decomposition of additives during battery preparation.

linear increase with temperature. This parameter was introduced since the analogue is presented for battery weight loss in Fig. 7(b). The batteries were weighed in regular intervals during charging (see Fig. 7(a)). Exponential behaviour of weight loss m_{Loss} with charge time is observed for all temperatures ($R^2 \geq 0.95$, boundary condition $m_{Loss}(t=0)=0$). Of course, the charge current does not contribute to any electrochemical energy in the battery, but merely drives electrolysis of the electrolyte. The exothermal internal oxygen recombination results in additional temperature increase. Thus, oxygen, hydrogen, water vapour and gaseous decomposition products escape from the unidirectional valves in the lid. More than m_{Loss} = 500 g was reached in the investigation (for 90 Ah AGM batteries). For example, the nine-fold C_{nom} was charged in case of the T = 60 °C battery. The weight loss rate also shows exponential behaviour with temperature as can be seen in Fig. 7(b).

A short estimation demonstrates the relevance of the presented experiment. In case of T = 40 °C, after 700 h of charging with U = 14.8 V about 100 g weight loss were measured. Then, the degree of saturation of AGM separators and plates with electrolyte is lowered by about 2%. At worst-case assumption, which is that any battery refresh takes place solely at T = 40 °C and takes the maximum duration of 50 h, a comparable weight loss is reached after about 22 refresh chargings, i.e. around 132 full cycles in the vehicle. Of course, weight loss to such an extent and without any other aging side effects is unlikely in customer operation. Nevertheless, the effects of weight loss in AGM batteries on critical battery parameters have to be considered. This was partially accomplished in [11] before. Seventeen 90 Ah AGM batteries were subjected to different weight losses by overcharging. Then, the batteries were tested in terms of C_{20} capacity (see Fig. 8(a)), internal resistance (see Fig. 8(b)) and cold cranking performance according to EN 50342-1 [32] (see Fig. 8(c) and (d)). The t_{6V} parameter shows strong relation to weight loss (see Fig. 8(c)). However, especially this observation is related to the way of battery preparation by overcharging. Due to elevated temperature and voltage not only water loss occurs, but also irreversible decomposition of specific additives in the active masses, which ensure high t_{6V}. In common vehicle operation these additives are expected to withstand overcharge intervals. In contrast, there is only a minor impact of water loss on the C_{20} capacity (see Fig. 8(a)), which comes from the low discharge current during the capacity measurement [11]. The capacity depends primarily on the absolute content of HSO_4^- ions, which does not change with weight loss. If the current is low enough, these ions participate in the discharge reaction after diffusion to the reaction site. However, the kinetics of these processes decelerates with lower degree of saturation due to limited ion transport, so that the 6 V discharge limit (see DIN EN 50342-1 [32]) is reached disproportionately earlier under high discharge rates. Both corrosion of the positive grid and degradation of the PAM support this effect. The increase in internal resistance R_i (b) and the decay of the cold cranking voltage U_{10s} (d) are also important, see also [11]. These parameters have a critical impact on ASSF. The effects are moderate so that a high weight loss of m_{Loss} = 250 g is necessary to effect a drop below $U_{10s} \leq 7.5$ V during a cold crank, which is the specification for brand-new batteries [32]. According to the example mentioned above (m_{Loss} = 100 g at 132 fc) this corresponds to more than 300 fc. Of course, this statement refers to only one single aging phenomenon and ignores the complexity of interacting aging phenomena.

To sum up this section, regular battery refresh outside of the optimum temperature-dependent charge voltage characteristics does not cause weight loss to such an extent that functionality of VRLA–AGM batteries is significantly lowered during cycle life in the MHPS application. However, it has to be noticed that this statement may not be valid for batteries mounted in the engine compartment without any thermal shielding. Additional water evaporation at elevated temperature is out of the scope of this work.

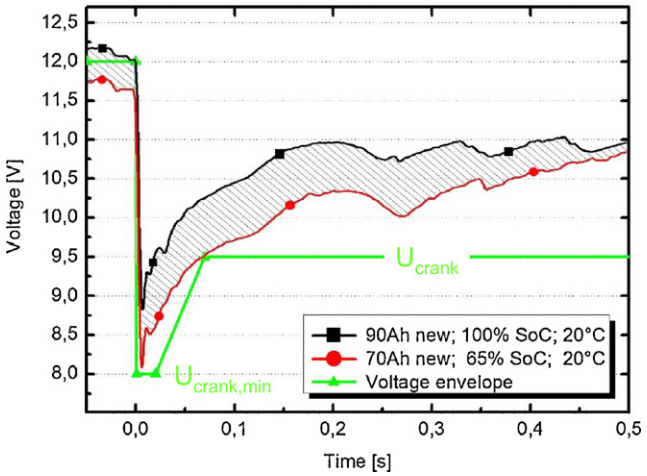

Fig. 9. Typical voltage characteristics during an ASSF warm crank for two different VRLA–AGM batteries mounted in the same test vehicle. The initial voltage drop is followed by first cylinder compressions in the range of a few hundred ms. The voltage drop of the battery is determined by its internal resistance.

4. Warm cranking performance

The main requirement for the VRLA–AGM battery in ASSF application is reflected by power net stability during warm cranking after an idling stop. During cranking the availability of critical features like safety systems, assistance systems and infotainment must not be influenced negatively. Therefore, specific voltage parameters, U_{crank} and $U_{crank,min}$, must not be undercut during cranking (see Fig. 9). These voltage limits are shown by two exemplary warm cranks (six-cylinder Diesel engine) following a 75 A-load for 30 s (simulation of an idle stop). The initial voltage drop is caused by a temporary battery short circuit through the armature winding of the starter and is followed by voltage relaxation, which is superposed by single cylinder compressions as long as the crankshaft is towed. For example, it is seen that a brand-new 70 Ah battery at SoC = 65% and 20 °C battery temperature is at the outer limit for ensuring power net stability during cranking. However, the challenge in system design and validation is not to develop the best possible ASSF functionality for a brand-new vehicle, but to project the system to customer operation. Even after several months or years of operation with individual driving profiles, temperature and onboard power consumption, availability and reliability of ASSF have to be ensured. The battery internal resistance is the most critical parameter in this context. It determines the battery voltage behaviour at a defined high-rate load, e.g. an ASSF warm crank. The internal resistance is investigated for several batteries at different states-of-charge and temperature in this section. The load profile was simplified to a rectangular high-rate constant current signal for a duration of a few seconds with 540 A amplitude. This current is 60% CCA (cold cranking amps) of a 90 Ah AGM battery and part of the EN 50342-1 cold crank test [32]. The voltage response is evaluated at t = 40 ms after start trigger; this is in the rising slope between U_{crank} and $U_{crank,min}$ in Fig. 9. Shorter time scale was not reachable due to the control time of the used high-rate discharge tester. On the time scale of ms the internal resistance R_i comprises predominantly of the ohmic series resistance R_0; the electrochemical part of the total impedance $|Z|$ can be neglected in first approximation. The resistance R_0 comprises of the electric conducting components in the battery like active masses, grids and top lead and the ionic conductivity of the electrolyte. A linear impedance model consisting of only an ohmic resistance is supposed to produce acceptable results, which was confirmed also by Bohlen in similar experiments [33]. Thus, the

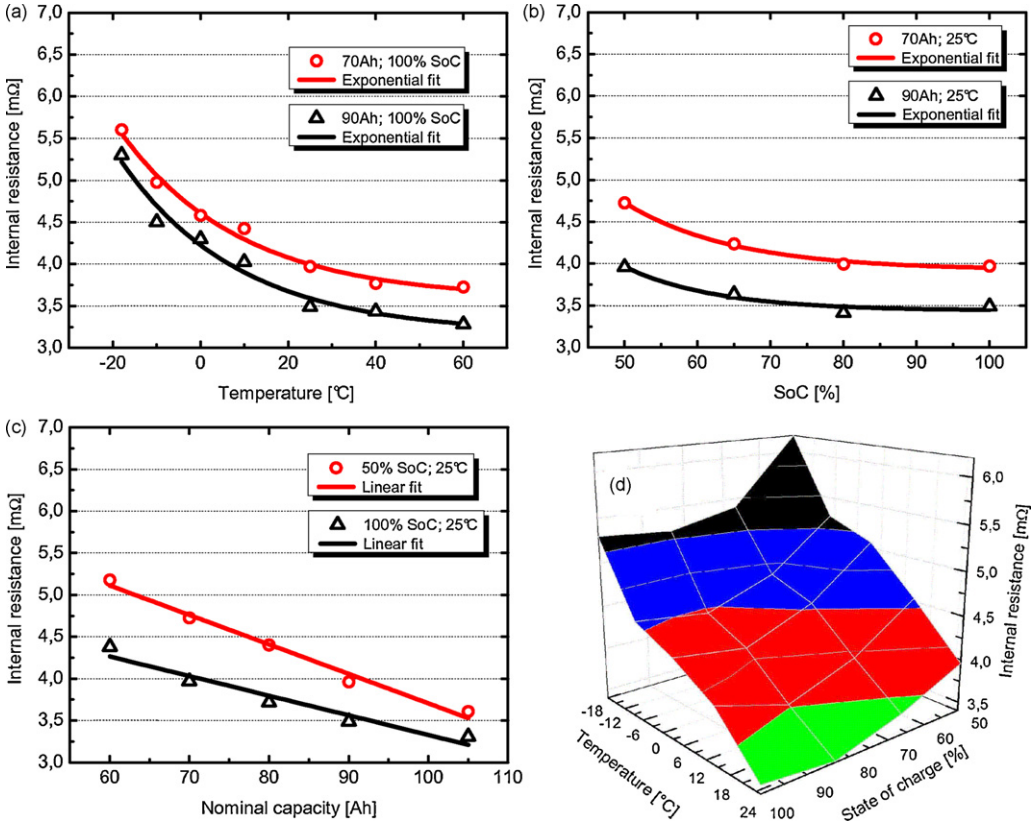

Fig. 10. Internal resistance of a 90 Ah AGM battery at high-rate discharge (540 A) for a square current pulse of $t = 40$ ms. The parameter space covers temperature (a), state-of-charge (b) and nominal capacity of the battery (c), whereby temperature has the greatest influence. A summary is given by the 3D-plot in (d).

internal resistance is calculated according to $\Delta U_{crank} = R_i I$ and is given in Fig. 10 for different conditions. The greatest influence on the initial battery internal resistance is given by temperature (a). According to Kurisawa and Iwata [34], the curves are dominated by the ionic resistance of the electrolyte, which compensates the increasing electric conductivity of the lead with decreasing battery temperature. The superposition of both effects results in an exponential behaviour. In the temperature range from −20 °C to 60 °C the internal resistance decreases by a factor of 1.5. As a result, the initial voltage in Fig. 9 would additionally drop by about 1 V. The 70 Ah VRLA–AGM battery reveals a similar characteristic at about 0.5 mΩ higher resistance compared to 90 Ah.

In Fig. 10(c) the measurement was performed with batteries of different nominal capacities. The discharge current was kept constant for all types of batteries. The EN standard battery sizes differ exclusively in container length, i.e. additional C_{nom} is reached by extra plates per cell. Therefore, the enlarged active surface collecting the current and the further amount of conducting material is responsible for lower initial resistance. The number of additional plates refers approximately linearly to the nominal capacity, which is confirmed by Fig. 10(c).

Compared to C_{nom} and temperature, battery SoC reveals the weakest impact (b). This is expected since the amount of reserve capacity is secondary for the pulse power performance. The decreased OCV at lower SoC induces the voltage minimum $U_{crank,min}$ to be lower by the same offset according to $U_{crank,min} = OCV - R_i I$. Two aspects are important concerning SoC: The increasing ratio of non-conductive lead sulphate becomes noticeable towards low state-of-charge. Towards full state-of-charge this effect is superposed by the conductivity of sulphuric acid in dependence of concentration at room temperature. It shows maximum conductivity at about 1.24 g cm^{-3}, i.e. SoC = 80%, with 0.82 Ω cm compared to 0.80 Ω cm at SoC = 50% and 0.78 Ω cm at SoC = 100%, respectively [29]. In total, there is no difference concerning initial internal resistance between a fully charged battery and a battery operated in the pSoC regime of BER. For a brand-new 90 Ah VRLA–AGM battery the internal resistance is summarized by a 3D surface plot in Fig. 10(d).

As was mentioned before, the most challenging aspect is to design the ASSF system taking battery aging into account. After months of operation in the field it has to be both highly available and reliable. The presented R_i-measurements were repeated with field-aged 90 Ah batteries. The batteries were operated in MHPS field test vehicles as described in [13,14]. The remaining capacity C_{act} of the chosen batteries was 40–80% C_{nom}. A number of 27 appropriate batteries of only one certified manufacturer were selected. In the presented experiment there was only a very weak correlation between R_i and C_{act}. In Fig. 11(a) the relative distribution of the internal resistance at room temperature is given as a histogram plot. A large scattering range is observed in the range from 3.3 mΩ to 4.2 mΩ. The scattering bandwidth justifies the previously explained, simplified evaluation according to the ohmic law. Of course, the deviation of a characteristic parameter for one cell σ_{cell} scales up to $\sqrt{6}\sigma_{cell}$ for the battery due to the laws of statistics [29]. Even basic parameters like the OCV at SoC = 100% reveal quite strong statistical (not systematic) scattering. Consequently, statistical distribution functions are used in order to describe battery behaviour. In most cases the normal distribution $y = y_0 + (1/(\sigma\sqrt{\pi/2}))\exp(-1/2((x - x_c)/\sigma)^2)$ can be used [29]. This function was fitted to the data in Fig. 11(a) ($R^2 = 0.77$). There is only scarce literature available that reports the statistics about aged batteries. Scattering phenomena of bat-

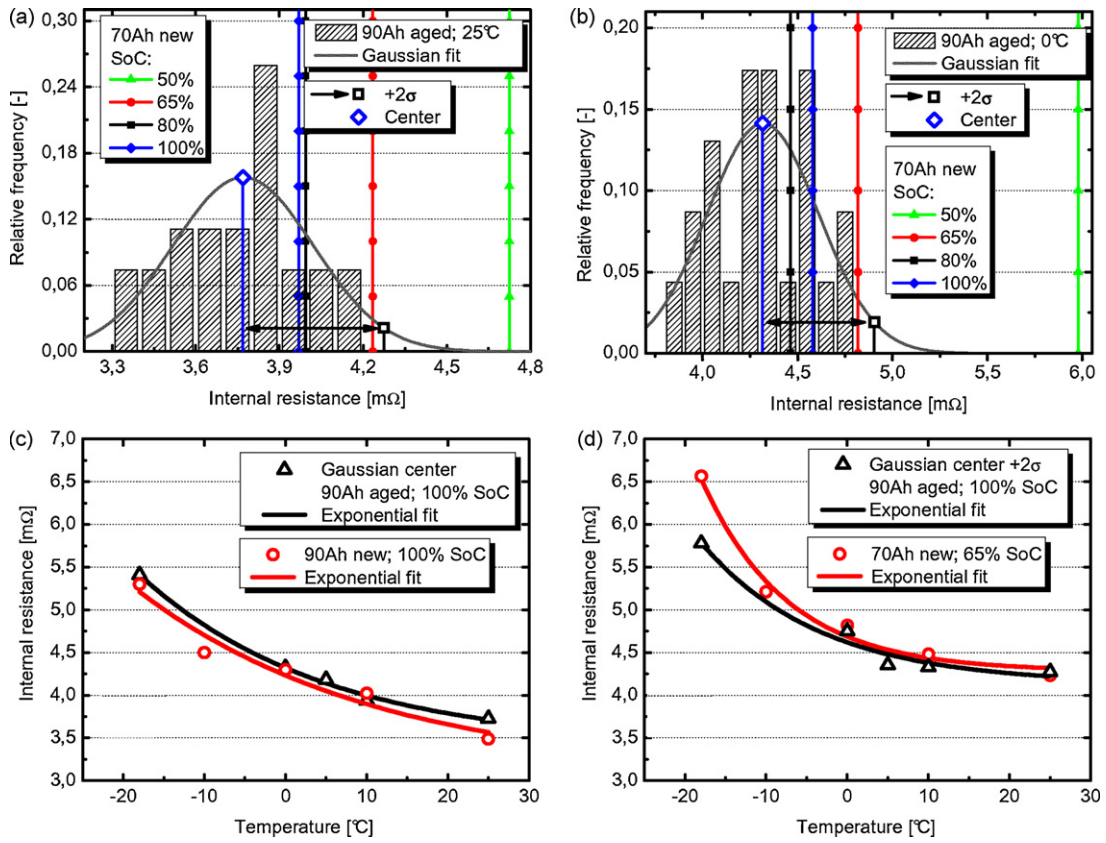

Fig. 11. The internal resistance of aged 90 Ah VRLA–AGM batteries (SoC = 65%) is characterised by strong scattering, which was fitted with a normal distribution (a and b). The +2σ-point of the Gaussian distribution matches with the internal resistance of new 70 Ah batteries at SoC = 65% in both cases. In (d) this comparison is given for the whole temperature range. The centre of the scattering area exceeds the internal resistance of new batteries by only 0.25 mΩ (c).

tery impedance are discussed, for example, by Hawkins and Hand [35] and by Toll and Moore [36]. They tested aged batteries for their remaining capacity and their conductance by ohmic measurements. The coefficient of determination was only $R^2 = 0.27$ (about 50 numbers of cases) due to extreme scattering in their experiment.

The vertical lines in Fig. 11(a and b) depict the average internal resistance of three brand-new 70 Ah batteries from the same supplier at different SoCs. Obviously, the SoC = 65% line matches the 2σ-point of the distribution in quite good agreement (3.77 mΩ + 2 × 0.253 mΩ). This means that only 2.5% of field-aged 90 Ah batteries may have a higher internal resistance than the brand-new 70 Ah battery conditioned to SoC = 65%, representativeness of the randomly selected test samples assumed. The centre of the distribution is about 0.25 mΩ above the average of three brand-new batteries (c). The analogous experiment was performed for the whole temperature range, as it was found in Fig. 10 that temperature has the most critical impact. Exemplary, the curves are shown for $T = 0\,^{\circ}C$ in (b) of Fig. 11 ($R^2 = 0.74$). Once more, the 2σ-point of the aged batteries is in accordance with the SoC = 65% of the 70 Ah batteries. In Fig. 11(d) it is confirmed that aged 90 Ah AGM batteries at full SoC are reproduced by 70 Ah batteries at SoC = 65% concerning the initial internal resistance over the whole temperature range in quite convincing agreement except for $T = -18\,^{\circ}C$. Thus, by conditioning a new battery, the ASSF system projection into the customer field can be done on the basis of simply reproducible instructions. Otherwise, 'representatively' or 'defined' aged batteries will have to be used, which is not easy to accomplish. Finally, it has to be noticed that the presented rule for simulating the customer field of used 90 Ah batteries only holds for the pulse charge performance, of course.

5. Deep discharge (overdischarge) robustness

The VRLA–AGM batteries applied in the MHPS are operated in a partially discharged state. The charge sustainment mode keeps the SoC in the range of around 80–85%. The decreased SoC level increases the probability for a VRLA–AGM battery to be deeply discharged (overdischarged). The charge reserve for long standing times or for operating conditions with strongly negative charge balance (e.g. short trip travelling) is about 10% lower compared to the conventional power net. When operation is continued out of the deep discharged state, the power management may switch to battery refresh mode with 14.8 V charge potential [5]. A further aspect is problematic in this context: VRLA–AGM batteries are acid-limited and in the deeply discharged state the acid concentration in these batteries converges to nearly 1.0 g cm^{-3}. Thus, the solubility of $PbSO_4$ is increased and the recrystallisation process introduced in Section 2 is strongly activated. This results in crystal growth of dendrites of lead sulphate, which may bridge the oppositely polarized electrodes. The stability of the formed dendrites is supported by the absorbent glass mat. Although subsequent charging dissolves the lead sulphate dendrites at their thinnest spots, there is exceptionally high electric field strength at the location of the dendrites' stumps. Hence, the active masses preferably form at the former site of the non-conducting dendrite and generate a conducting channel across the electrodes. The consequence is a micro-short circuit. In Fig. 12(a) and (b) an outlier example for such micro-circuits is given. The affected cells do not contribute to the electrochemical potential any more. Instead, the remaining cells experience a higher charge voltage, which causes electrolysis and evaporation of the electrolyte. Therefore, the exothermal recombination process is promoted in VRLA–AGM batteries. The shift of the activity from

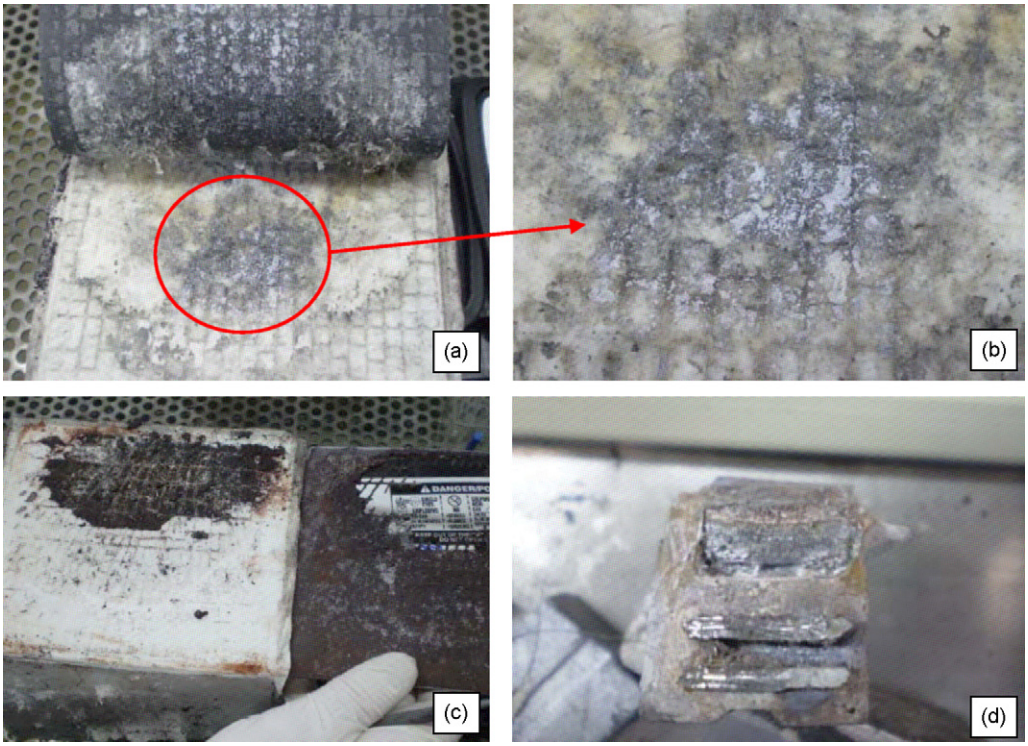

Fig. 12. Tear-down analysis of a deeply discharged battery (battery type #2): The separator material shows micro-shorts in the centre region (a and b). (c) Symptoms as known from strongly overcharged batteries are observed at the upper part of the positive grid. The AM has hardened and the grid material is extremely brittle. Corrosion was also found at the cast-on strap and the lugs of the positive plates (d).

main to side reactions may inhibit complete transformation of the discharged material. At unfavourable conditions the requirements for a thermal runaway might even be reached.

For the majority of costumers the probability for a vehicle breakdown due to a deep discharge (and not the following charging) is much more serious, of course. This is why modern SLI batteries are designed preferably robust. This is realized by, firstly, optimized low self-discharge rates and, secondly, suppressed growth of dendrites by addition of Na_2SO_4 to the electrolyte. Sodium sulphate reduces the solubility product $c(Pb^{2+}) \times c(SO_4{}^{2-})$ and decelerates the recrystallisation process. Both measures determine the possible duration of a VRLA battery at deep discharge conditions before damage occurs.

The robustness against deep discharge (overdischarge) is tested in this section. For this purpose a cycle test according to Table 1 was designed by BMW. It consists of repeated deep discharge and full charge cycles. Deep discharge is reached by connecting a light bulb of 10 W for 7d to the battery directly after a C_{20} capacity test. Thus, the voltage drops to OCV $\leq$ 1–3 V. Subsequently, the battery is fully *IU*-charged with maximum current I_4. The test is especially sensitive to the degree of saturation of the AGM material with electrolyte, the plate pressure and the internal recombination efficiency. Further details of the electrochemical mechanisms and effects of the 'overdischarge' test are reported in [37].

Battery types of different suppliers that were released or in the approval process (only 90 Ah batteries) were used for the test. In Fig. 13 the results according to the test regime in Table 1 are presented. The development of C_{act} is shown in (a) (step 2 in Table 1), the final charge current $I_{finalchg}$ (step 4 in Table 1) is given in (b). At the development stage of the deep discharge test, battery type #4 suffered from a design weakness. The battery was underfilled by 3% in relation to the nominal saturation level with acid of too low specific gravity. Then, acid limitation of a VRLA battery is aggravated, which results in lower capacity as was seen already in Section 3 of this article. Furthermore, the growth of dendrites is activated earlier with decreasing SoC and the recombination rate is increased by a higher number of gas channels across the plates. The behaviour of battery type #4 matches with these effects, already having an initial lack of C_{20} capacity (see Fig. 13(a)). After the first deep discharge cycle, the final charge current is already 7 A (b) with a subsequent capacity loss of 50%. Another problem concerned the separator material of this battery type. The tortuosity of the AGM was chosen too low. Also the robustness against damage as a result of deep discharge is determined by the tortuosity of the separator. Dendrites can form more easily if the AGM microstructure is less tortuous. Two samples of battery type #2 were tested. One of the batteries resulted in a thermal runaway after the second deep discharge cycle (ring symbols in Fig. 13). The *IU*-charge had to be stopped after about 8 h since the charge current was kept at its upper limit and the surface temperature of the battery container exceeded $T = 50\,^{\circ}C$. Escape of electrolyte occurred even through the gassing channel of the lid. In the final TDA (see Fig. 12) slightly melting of the valves and 1.6 kg weight loss was found. The centre of the separators was perforated with visible dendrites (a and b) forming micro-short circuits and the active masses were extremely hardened. As it is typical of heavily overcharged batteries, the positive grids were extremely corroded especially in the upper third (c). Corrosion was also observed at the positive cast-on strap (d). The particular root cause for the onset of the thermal runaway could not be clarified. Also a manufacturing defect like a fine built-in short circuit could be possible. It was known from battery type #2 that it constructively suffered from too low plate pressure, which agrees with the significantly different behaviour of the second sample of this battery type. As it could be expected, it showed a comparable behaviour to the flooded battery, which was tested as a reference. Since flooded batteries react without internal recombination and since the formation of micro-shorts can be excluded due to the missing stabilizing medium, the final charge current stays at a low level up to 18 cycles and essentially promotes the gassing reaction only. However, flooded batteries suffer from enhanced capacity

Table 1
Profile for testing the deep discharge (overdischarge) robustness of VRLA–AGM batteries as introduced by BMW.

Deep discharge test: $T = 25\,^{\circ}C$			
Step		Type	Parameters
1		*IU*-Charge	$U = 14.8$ V $I = 5I_{20}$
2	Repeat until $I_{finalchg} \geq 8$ A (step 4)	Discharge	$I = I_{20}$ $U = 10.5$ V
3		Deep discharge	10 W light bulb for 7d
4		*IU*-Charge	$U = 14.8$ V $I = 5I_{20}$

loss due to stratification and sulphation of the lower parts of the plates. Furthermore, the mechanical stress on the AMs which stems from volume variations during charging and discharging has a more serious impact on flooded batteries and results in shedding and mossing. The batteries of type #1 and #3 reveal the behaviour of well-designed VRLA–AGM batteries in the deep discharge test. Both types have lost not more than one third of their nominal capacity at the end of the test.

During the first cycles of deep discharge the charge factor is constant at the high level of 1.5–1.6 (see Fig. 13(c)). This is linked to the OCV of ≤1–3 V after step 3 in Table 1 and the end of discharge criterion of 10.5 V in step 2. As soon as the battery loses some electrolyte after a few deep discharge cycles, the recombination rate and the charge factor increase further which is accompanied by the formation of micro-shorts at the end of the test. In Fig. 13(d) the charge curve according to step 4 in Table 1 is compared before and after the test for battery #1. It can be seen that the first quarter of the charge procedure is almost congruent in both cases. During initial electrochemical charging, the lead sulphate dendrites are converted to conducting bridges between the plates. Consequently, the concerning cells are not charged any more and the turning point in charge current is responsible for battery heating and further current increase. This interpretation is confirmed by the TDA of battery type #1 as presented in Fig. 14. Corrosion could be hardly found at the positive plates since the overcharge in part (d) of Fig. 13 was interrupted after 12 h. Instead, an inhomogeneous lead sulphate distribution was found across the NE. The lower part of the NE revealed sulphation (Fig. 14(a)), whereas the upper part still featured the luster of lead. In the same area the separator is frequently punctured by active material, which caused battery failure.

Since the risk of a deep discharge increases in the MHPS, BMW has defined that a battery has to withstand 9 deep discharges with

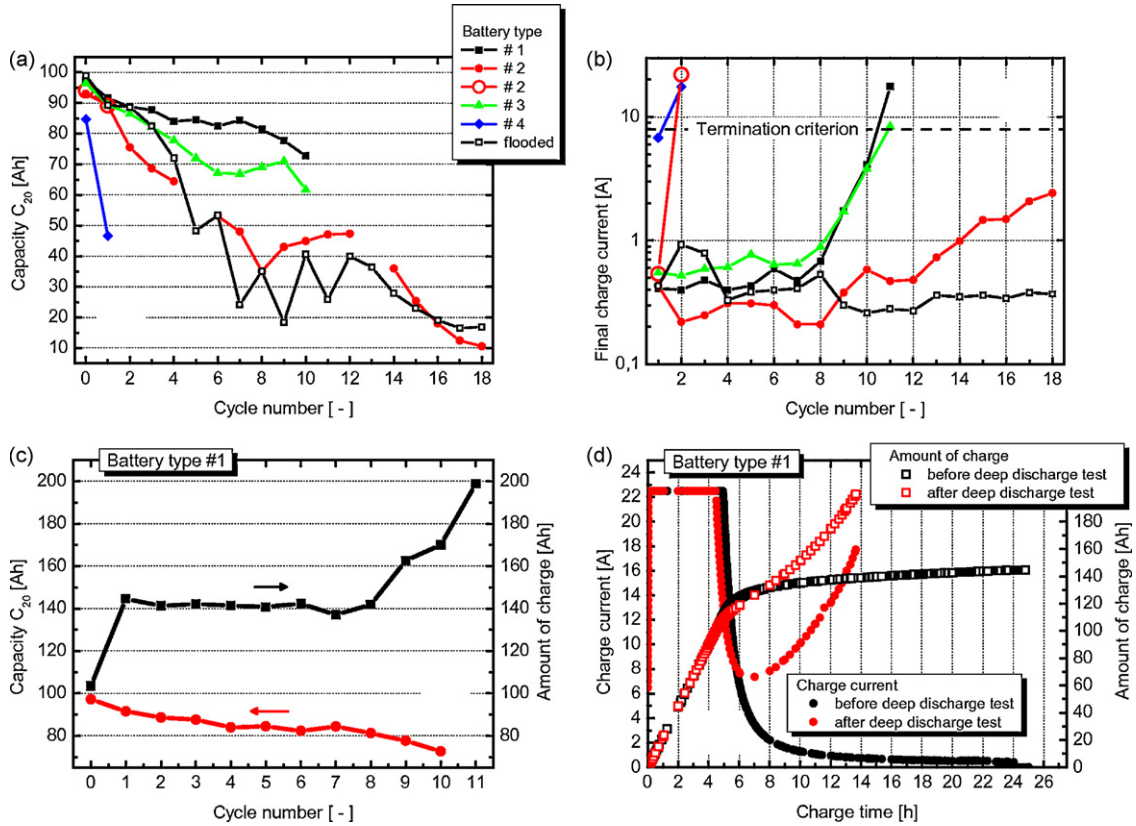

Fig. 13. The 7d-deep discharge (overdischarge) test was performed for four AGM battery types and a conventional flooded battery. Concerning the C_{20} capacity, a strong scattering was observed for the AGM batteries in terms of degradation (a). (b) Battery type #4 was underfilled, which resulted in an increased final charge current already after the first deep discharge cycle. Battery type #2 suffered from low plate pressure and, thus, behaves similar to a flooded battery. In contrast, types #1 and #3 represent well-designed VRLA–AGM batteries. The charge factor is larger than 1.5 after deep discharge (c, exemplary for type #1) as the batteries are fully charged from OCV ≤ 1–3 V and discharged to 10.5 V in the capacity test. (d) Within the first 6 h of *IU*-charging following a C_{20}, the charge current is similar. This was done before and after the test for battery #1. Only after 6 h, the charge current escalates and reaches the test termination criterion due to high recombination rates and micro-shorts.

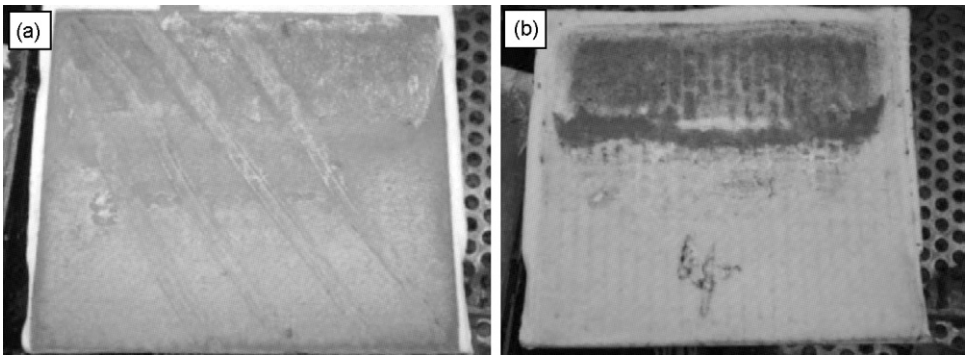

Fig. 14. For battery type #1 a TDA was carried out: (a) sulphation was detected only in the lower part of the surface area of the negative plate, the upper part still featured the metallic luster of lead. (b) The separators were punctured by $PbSO_4$ in the upper part.

at least $C_{act} = 66\%\ C_{nom}$ according to the 7d test. This demonstrates that flooded batteries are not appropriate despite the low final charge current. But low charge voltage out of the deep discharged state strongly favours acid stratifications in flooded batteries.

Furthermore, substantial differences are currently prevalent in the VRLA–AGM battery market.

6. Summary and outlook

Selected key parameters for operating LA batteries in the MHPS were investigated.

High efficiency of boost charging during BER requires high DCA. It is found that the DCA deteriorates significantly with extended vehicle rest times due to recrystallisation of lead sulphate. By refresh charging the DCA can be re-activated.

Due to the battery refresh and the boost charging at elevated voltage independent of temperature, the LA batteries have to be robust against water loss. This is very critical for valve-regulated LA batteries since the saturation of the separator with electrolyte is a sensitive parameter. However, it is demonstrated that this issue is not expected to become a serious problem during battery cycle life if the batteries are mounted in the trunk.

Low internal resistance is critical for ASSF, as the LA batteries have to withstand many high-rate discharges due to warm cranks. For reasons of power net stability the voltage drop has to be kept small. By measuring a reference group of aged batteries, it is demonstrated that the internal resistance shows significant scattering, but less than 10%. This makes system validation of ASSF quite challenging and prompts the demand for 'defined' aged batteries.

Finally, the probability of deep discharges is increased in the MHPS due to the pSoC operational strategy. The robustness against deep discharges is reflected by the frequency of deep discharges and re-charges the battery can withstand. Significant differences were found for different designs of valve-regulated LA batteries in AGM technology.

In part II of this publication an accelerated cycling procedure is presented by which the key parameters of LA battery operation in the MHPS are reflected as far as possible.

Acknowledgements

We gratefully thank H. Koch (Combatec GmbH) for constructive cooperation with TDAs, H. Döring (ZSW Ulm) and E. Meissner (Johnson Controls Power Solutions EMEA) for fruitful discussion and F. Plunien (BMW AG) for programming support.

References

[1] S. Wolff, D. Abendroth, W. Weigl, C.-P. Linner, R. Neudecker, M. Schneider, W. Huber, A. Rau, Proceedings of the 7th Stuttgart International Symposium 'Automotive and Engine Technology', Stuttgart, Germany, March, 2007.
[2] M. Hafkemeyer, F. El-Dwaik, A. Heim, J. Liebl, J. Stauber, F. Traub, Proceedings of the 12th International Conference on Electronic Systems for Vehicles, Baden-Baden, October 6–7, 2005.
[3] M. Schmid, in: M. Schöllmann (Ed.), Energiemanagement und Bordnetze II, Haus der Technik Fachbuch, Expert Verlag, Germany, 2007.
[4] S. Schaeck, Simultaneous engineering-based investigation of VRLA–AGM batteries in micro-hybrid electric vehicles, PhD thesis, to be published at Universität Ulm.
[5] S. Schaeck, A.O. Stoermer, E. Hockgeiger, Journal of Power Sources 190 (2009) 173–183.
[6] F. Dudenhöffer, M. Krüger, H. Schmaler, ATZ 106 (2004) 42–45.
[7] ADAC e.V. (German Automobile Club), ADAC Statistik Batteriepannen 1996 und 2006, March 2009, www.adac.de.
[8] T. Handschuh, Untersuchung des Betriebs- und Alterungsverhaltens von Blei-Säure-Akkumulatoren bei für Hybridantriebssystemen typischen Belastungen, PhD thesis, Universität Ulm, 2007.
[9] E. Karden, S. Ploumen, E. Spijker, D. Kok, D. Kees, P. Phlips, in: M. Schöllmann (Ed.), Energiemanagement und Bordnetze, Haus der Technik Fachbuch, Expert Verlag, 2004.
[10] D.U. Sauer, E. Karden, B. Fricke, H. Blanke, M. Thele, O. Bohlen, J. Schiffer, J.B. Gerschler, R. Kaiser, Journal of Power Sources 168 (2007) 22–30.
[11] J. Albers, Journal of Power Sources 190 (2009) 162–172.
[12] A. Cooper, J. Furukawa, L. Lam, M. Kellaway, Journal of Power Sources 188 (2009) 642–649.
[13] S. Schaeck, T. Karspeck, C. Ott, M. Weckler, A.O. Stoermer, A field operational test on VRLA–AGM batteries in micro-hybrid electric vehicles. Part I. Results based on Kernel Density Estimation, Journal of Power Sources, accepted for publication.
[14] S. Schaeck, T. Karspeck, C. Ott, D. Weirather-Koestner, A.O. Stoermer, A field operational test on VRLA–AGM batteries in micro-hybrid electric vehicles. Part II. Results based on multiple regression analysis and tear-down analysis, Journal of Power Sources, (2010) doi:10.1016/j.jpowsour.2010.08.101.
[15] D. Pavlov, T. Rogachev, P. Nikolov, G. Petkova, Journal of Power Sources 191 (2009) 58–75.
[16] P.T. Moseley, R.F. Nelson, A.F. Hollenkamp, Journal of Power Sources 157 (2006) 3–10.
[17] P.T. Moseley, Journal of Power Sources 191 (2009) 134–138.
[18] M. Shiomi, T. Funato, K. Nakamura, K. Takahashi, M. Tsubota, Journal of Power Sources 64 (1997) 147–152.
[19] M. Thele, J. Schiffer, E. Karden, E. Surewaard, D.U. Sauer, Journal of Power Sources 168 (2007) 31–39.
[20] Y. Yamaguchi, M. Shiota, Y. Nakayama, N. Hirai, S. Hara, Journal of Power Sources 93 (2001) 104–111.
[21] Y. Yamaguchi, M. Shiota, M. Hosokawa, Y. Nakayama, N. Hirai, S. Hara, Journal of Power Sources 102 (2001) 155–161.
[22] Y. Yamaguchi, M. Shiota, Y. Nakayama, N. Hirai, S. Hara, Journal of Power Sources 85 (2000) 22–28.
[23] H. Bode, Lead-Acid Batteries, J. Wiley & Sons, 1977.
[24] D.U. Sauer, Optimierung des Einsatzes von Blei-Säure-Akkumulatoren in Photovoltaik-Hybrid-Systemen unter spezieller Berücksichtigung der Batteriealterung, PhD thesis, Universität Ulm, 2003.
[25] W. Kappus, Electrochimica Acta 28 (11) (1983) 1529–1537.
[26] M. Thele, A contribution for the modelling of the charge acceptance of lead-acid batteries – using frequency and time domain based concepts, PhD thesis, RWTH Aachen, 2007.
[27] E. Meissner, Private communication, April 29, 2009, Hannover.
[28] H. Döring, Private communication, June 25, 2009, Stuttgart-Weilimdorf.
[29] D. Berndt, Bleiakkumulatoren, VDI-Verlag, Düsseldorf, 1986.
[30] D. Pavlov, P. Nikolov, T. Rogachev, Journal of Power Sources 195 (2010) 4444–4457.
[31] D. Pavlov, P. Nikolov, T. Rogachev, Journal of Power Sources 195 (2010) 4435–4443.

[32] DIN EN 50342-1, Lead-acid starter batteries – general requirements and methods of test, November 2006.
[33] O. Bohlen, Impedance based battery monitoring, PhD thesis, RWTH Aachen, 2008.
[34] I. Kurisawa, M. Iwata, Proceedings of the 19th International Telecommunications Energy Conference INTELEC, 1997.
[35] J.M. Hawkins, R.G. Hand, Proceedings of the 18th International Telecommunications Energy Conference INTELEC, 1996.
[36] R.Z. Toll, M.R. Moore, Proceedings of the 24th International Telecommunications Energy Conference INTELEC, 2002.
[37] A.O. Stoermer, S. Schaeck, E. Hockgeiger, Design verification of VRLA–AGM batteries, Journal of Power Sources, in preparation.